Electrical Power and Energy Systems 172 (2025) 111328

Contents lists available at ScienceDirect

International Journal of Electrical Power and Energy Systems

journal homepage: www.elsevier.com/locate/ijepes

Weight minimization of electric vertical takeoff and landing aircraft: From the comprehensive powertrain perspective

Zeyu Cheng [a], Zhi Cao [a], John T. Hwang [b], Chris Mi [a,*]

[a] San Diego State University, 5500 Campanile Dr, San Diego, 92182, CA, USA
[b] University of California San Diego, 9500 Gilman Dr, La Jolla, 92023, CA, USA

ARTICLE INFO

Keywords:
UAM
eVTOL aircraft
Powertrain modeling
Optimization

ABSTRACT

This paper proposes a conceptual design optimization method for the powertrain of electric vertical takeoff and landing (eVTOL) aircraft. The converter selection, semiconductor device selection, inductor design, capacitor selection, and thermal management design are discussed. The detailed analysis of various losses, including semiconductor losses, magnetic component losses, and auxiliary electronics losses, is illustrated. Moreover, the hybrid optimization algorithm is utilized to address the problem of multiple local optima. A configuration study with a 30km cruise mission range is implemented to analyze the variation of each design variable in the optimization. Additionally, a comparison study is conducted to assess the impact of powertrain system design on eVTOL aircraft. The proposed method achieves up to a 4.3% reduction in gross mass and an 8.8% reduction in required battery energy, highlighting the significance of incorporating powertrain modeling in aircraft-level optimization. Finally, sensitivity analysis is presented with respect to the mission range. This paper bridges the gap in current eVTOL design methodologies from a powertrain perspective, further reducing gross mass and providing guidelines for powertrain design in eVTOL aircraft.

1. Introduction

In recent years, Urban Air Mobility (UAM), a potential future air-taxi service, has gained widespread attention in academia and industry, due to increased traffic congestion and growing concerns about gas emissions. In UAM services, electric vertical take-off and landing (eVTOL) aircraft would primarily be used for short-distance transportation of less than 100 kilometers [1,2]. The eVTOL aircraft offers several advantages over conventional aircraft, including environmental benefits, noise reduction, reduced maintenance costs, and time savings during commutes [3]. Therefore, these significant benefits of eVTOL aircraft have motivated extensive research.

Table 1 lists the prior work and their limitations. Many researchers studied the preliminary design and optimization of eVTOL aircraft with different objectives [4–8]. [4] developed a tool focusing on the mechanical aspects of conceptual design and optimization for eVTOL aircraft. The cost per trip was used as the objective function, and several eVTOL configurations were compared and studied. This author highlights that the keys to cost reduction in UAM services are to implement autonomous driving, extend battery life, and reduce battery manufacturing costs. The study by [6] modeled and optimized eVTOL aircraft using a gradient-based optimization method, emphasizing on parameter sensitivity analysis of rotor and aerodynamic. The study described in [7] implemented an eVTOL trajectory optimization with a physics-based model. This model accounted for several factors, including rotor aerodynamics, wing aerodynamics, motor performance, and acoustics. These paper focus on the multidisciplinary system-level design and optimization for eVTOL aircraft, considering disciplines such as aerodynamics, battery, motor, acoustics, and structures. However, these studies examine the performance of eVTOL aircraft without using a powertrain system model or by using simplified powertrain models during optimization, which considerably reduces the practical value for both industry and researchers.

Some studies, [9,10], optimize the powertrain system with respect to multiple performance criteria (efficiency, power density, and costs). In [9], a multi-objective pareto optimization was implemented. Five DC/DC converters were optimized and compared. [10] presents a design methodology for high power density inverter, emphasizing on the weight minimization. However, these studies concentrate only on optimizing the powertrain itself, while neglecting the impact of the powertrain system on the eVTOL aircraft. Regarding powertrain optimization, it is insufficient to solely focus on the efficiency and power density of the powertrain alone. Given that the powertrain mass contributes only a small percentage of the total mass of the aircraft, it is

* Corresponding author.
E-mail address: cmi@sdsu.edu (C. Mi).

https://doi.org/10.1016/j.ijepes.2025.111328
Received 4 December 2024; Received in revised form 22 October 2025; Accepted 26 October 2025
Available online 1 November 2025

Table 1
Existing research review

Reference	Objective	Limitations
[4]	Minimize eVTOL cost per trip	Constant powertrain efficiency
[5]	Minimize eVTOL operating cost	Constant efficiency and mass
[6]	Maximize range	No powertrain model
[7]	Minimize required battery energy	No powertrain model
[8]	Minimize eVTOL gross mass	No powertrain model
[9,10]	Maximize inverter efficiency and power density	Low-fidelity powertrain model
Proposed Model	Minimize eVTOL gross mass	

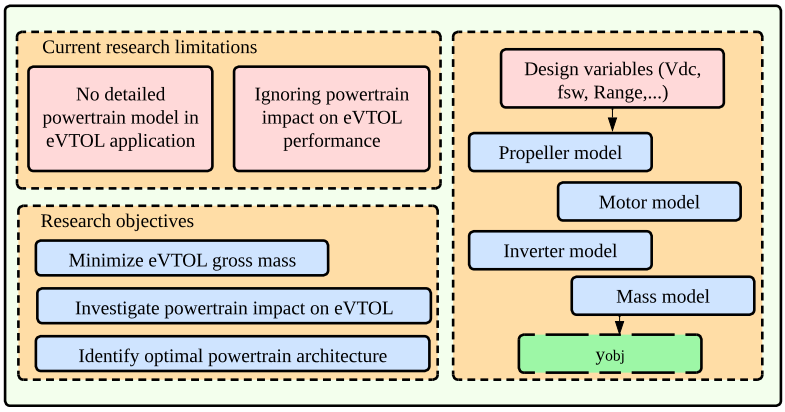

Fig. 1. Powertrain system.

more valuable to consider its effect on other components of the eVTOL aircraft, such as the battery mass and the energy distribution for the entire mission. [11] proposes a generic design methodology for VTOL aircraft with hybrid-electric propulsion systems, aiming to maximize the mission range under fixed gross weight and payload constraints. However, this study focuses on system-level configuration optimization and does not include detailed powertrain modeling or off-design performance analysis. [12] proposes a multidisciplinary design optimization framework for eVTOL aircraft, integrating aerodynamics, propulsion, and structural models to achieve overall performance improvement. However, this study mainly focuses on aircraft-level optimization and does not consider the detailed design and loss modeling of power electronic converters within the powertrain system.

This paper aims to present and discuss the results and findings from the conceptual design of UAM vehicles, with a particular emphasis on electric powertrain architectures. The following research questions will be addressed:

(1) What is the impact of powertrain architecture on the design of eVTOL aircraft?

(2) How to systematically identify the optimal powertrain architecture in eVTOL aircraft?

(3) How can the key design variables in powertrain architecture for eVTOL aircraft be effectively identified and selected?

The objective in this paper is to minimize the gross mass of eVTOL aircraft by developing an in-depth powertrain model and mission model. Furthermore, this paper conducts a comparison between the optimization results and a reference model that lacks a powertrain component. The purpose is to evaluate the influence of powertrain modeling on the performance of eVTOL aircraft. Finally, a design methodology for powertrain modeling is presented as a guide for non-experts in powertrain modeling. Fig. 1 provides a graphical abstract, summarizing the core research background, research objective, and methodology of this work.

This paper is organized as follows: Section 2 presents a design methodology for the powertrain model, including the selection of converter topologies, design of inductor, and modeling of the remaining components. Section 3 presents the optimization routine, mass model, and mission profile model. The model validation, comparison, and parameter sensitivity analysis are given in Section 4. Finally, conclusions are presented in Section 5.

2. Powertrain modeling methodology

The following sections describe the design and modeling methodology for converter topologies, semiconductor, inductor, capacitor, and cooling system. Fig. 2 illustrates the schematic of the powertrain system analyzed in this study. The powertrain system follows the architecture used in all-electric aircraft (AEA) [13]. The battery pack connects to the inverter, which then connects to the motor. It should be noted that the motor is not included in this powertrain architecture, due to its complex modeling methodology.

2.1. Power converter topology selection

Based on the configurations, sizes, and power demands of eVTOL aircraft, choosing different converter topologies and powertrain architecture is extremely important. Fig. 3 depicts the main schematic of the studied topologies.

Three inverter topologies are evaluated in this paper: Two-level (2L) inverter, Three-level Active Neutral Point Clamping (3L-ANPC) inverter, and Three-level T-type (3L-T) inverter, presented in Fig. 3(a), Fig. 3(b), and Fig. 3(c), respectively. All inverter topologies are operated using Sinusoidal Pulse Width Modulation (SPWM).

In the 3L-ANPC inverter, each leg has two active switches in series to share the block voltage. This configuration is beneficial in high-voltage applications, especially when the maximum acceptable voltage stress of devices available in the market is less than the voltage rating of the application. Apart from that, a significant advantage of the 3L-ANPC inverter is that two devices in each phase operate at the base electrical frequency, which reduces the switching losses compared to the conventional 3L-NPC inverter. However, the series connection in each leg leads to increased conduction losses in the 3L-ANPC inverter.

In contrast, the 3L-T inverter has advantages on the total number of devices and less conduction losses. This is due to the fact that each leg in the 3L-T inverter contains only one device rather than two series in

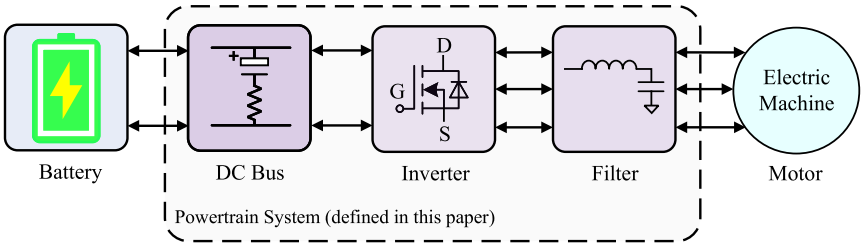

Fig. 2. Powertrain system.

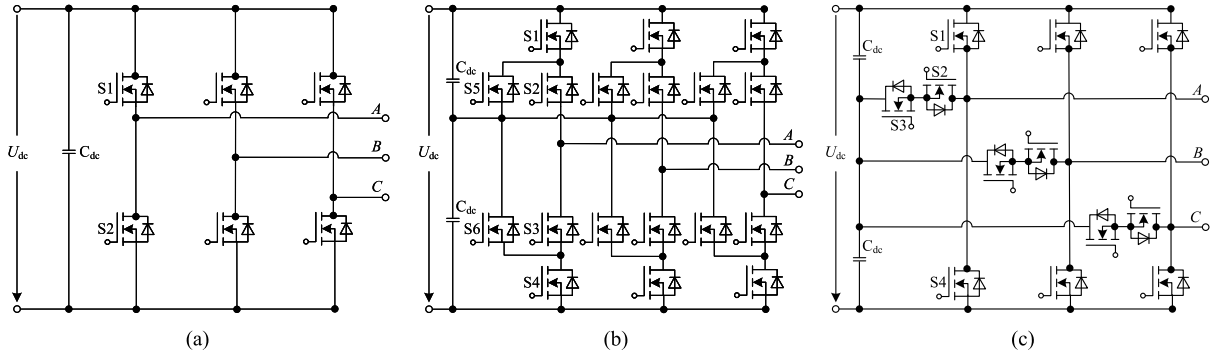

Fig. 3. Main considered converter topologies: **(a)** Two-Level inverter, **(b)** Three-Level ANPC inverter, **(c)** Three-Level T-type inverter.

Table 2
Semiconductor devices used in this study

Mfr.Part	Mfr.	Tech.	$V_{ds,max}$	R_{on}	I_d	$R_{th,j}$	C_{oss}	$t_{on}+t_{off}$
G3R12MT12K	GeneSiC	SiC	1.2 kV	12 mΩ	157 A	0.26 °C/W	284 pF	56 ns
BSM180D12P2C101	Rohm	SiC	1.2 kV	11 mΩ	204 A	0.11 °C/W	1500 pF	160 ns
TP65H015G5WS	Transphorm	GaN	650 V	18 mΩ	93 A	0.47 °C/W	307 pF	27.4 ns
GA50JT06–258	GeneSiC	SiC	600 V	25 mΩ	100 A	0.26 °C/W	284 pF	77 ns
IGO60R070D1AUMA1	Infineon	GaN	600 V	70 mΩ	31 A	1 °C/W	72 pF	23 ns

other configurations. In the 3L-T inverter, the voltage stress on middle switches is only half of the dc-link voltage, allowing the use of lower voltage-rating devices. Due to the half voltage stress, the switching losses at middle switches are low. It should be noted that a series connection of two devices in each leg would be considered when a single device is insufficient to block the entire dc-link voltage.

2.2. Semiconductor model

As previously mentioned, depending on the aircraft specifications and converter topologies, different technologies and voltage rating semiconductors can be determined through optimization processes. In this paper, only Wide Bandgap (WBG) devices are studied, due to their high efficiency, high voltage rating, and high operating frequency. Table 2 lists all the power devices considered in this paper, along with their parameters. Note that the number of parallel or series devices is also considered during the optimization, as it affects the converter losses. The models for conduction losses and switching losses are presented below. All devices are assumed to operate at a constant temperature, and the mass of each device is assumed to be 6 g.

Conduction losses: The conduction losses P_{cond} are calculated as follows:

$$P_{cond} = I_{rms}^2 R_{ds,on} \tag{1}$$

Switching losses: The switching losses P_{sw} are calculated as follows:

$$P_{sw} = \frac{1}{2} C_{oss} V_{ds}^2 + \frac{1}{6} V_{ds} I_{rms} f_{sw} (t_{on} + t_{off}) \tag{2}$$

where $R_{ds,on}$ is the turn-on resistance of the semiconductor. C_{oss} is the output capacitance. t_{on} and t_{off} are the rise time and fall time, respectively. These four parameters are extracted from the semiconductor datasheet. V_{ds} is the drain–source voltage. f_{sw} is the switching frequency. I_{rms} is the rms current through the device. These three parameters depend on the working conditions and the selection of converter topologies.

2.3. Inductor model

The design of an inductor can be divided into two main components: magnetic component design and winding design. The magnetic component design is based on converter topologies, losses, and the reluctance model. In inverter applications, the inductor is primarily used as a filter to mitigate current ripple or the dv/dt ratio on the motor side. The value of the inductor depends on the ripple attenuation factor, power quality, and other design requirements. Based on the different converter topologies and applications, the inductor core shape and material could be different. Theoretically, the high power density of an inductor is mainly determined by the ratio of saturation flux density to mass density. Therefore, the amorphous material exhibits the highest power density compared to other materials [14]. However, the core losses of amorphous cores are relatively higher than those of other materials in high-frequency applications, due to their high saturation flux density [15,16]. For these reasons, different core materials are compared and selected based on the various converter topologies and operating conditions.

The inductor geometry is divided into separate regions to build a reluctance network, as shown in Fig. 4(a). The magnetic equivalent circuit (MEC) model of a three-phase inductor is present in Fig. 4(b). A non-linear iteration method is adopted in the MEC model to calculate the magnetic flux density in different regions, as shown in Fig. 4(c).

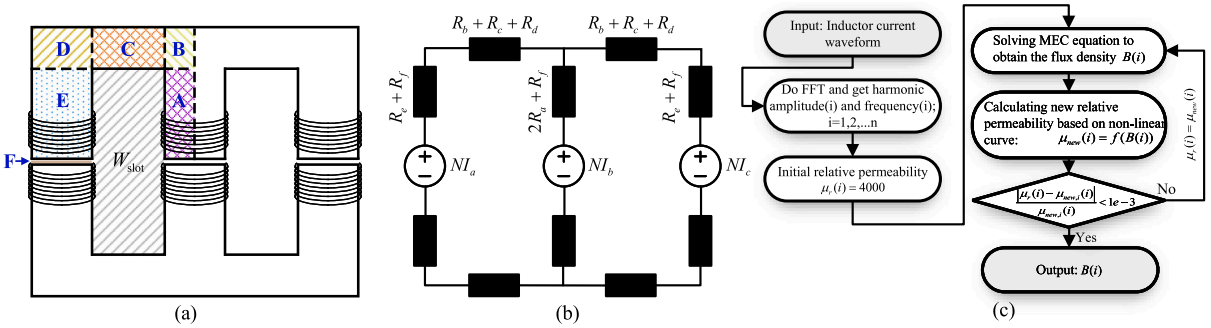

Fig. 4. (a) EE core geometry for reluctance calculation, (b) Magnetic equivalent circuit, (c) Non-linear iteration flowchart.

The improved generalized Steinmetz equation (iGSE) [17] is used to calculate the core losses P_{core} as follows:

$$P_{\text{core}} = \frac{1}{T}\int_0^T k_i \left|\frac{dB}{dt}\right|^2 (\Delta B)^{\beta-\alpha} dt \tag{3}$$

where α, β, and k_i are Steinmetz parameters [18,19]; ΔB represents the peak-to-peak magnetic flux density across each region.

The design of the winding depends on the current density, core shape, and saturation flux density. A constant current density is assumed to determine the winding diameters. The number of turns N is calculated using the maximum current $I_{\max}$, inductance L, saturation flux density $B_{\max}$, and cross-section area A_c, as shown in (4). The winding constraint equation can be given by (5), as the total copper area should be less than the slot area W_{slot}. The constant slotting factor K_s is assumed to be 0.7.

$$N = \frac{I_{\max} L}{B_{\max} A_c} \tag{4}$$

$$2N A_w \le K_s W_{\text{slot}} \tag{5}$$

The mass of the inductor is the sum of the selected core mass (determined by the core geometry and magnetic material) and the winding mass, which can be described by (6).

$$m_{\text{ind}} = m_{\text{ind,core}} + m\rho_m A_w N l \tag{6}$$

where m_{ind} is the mass of inductor, m represents the number of phases, ρ_m is the copper mass density, N is the number of turns, A_w is the area of a single conductor, and l is the length of one turn.

Litz wire is the only type considered in this study, due to its lower winding losses compared to other types of winding. The analytical model for winding losses, which takes into account the skin effect and proximity effect, is constructed following [20], as shown in (7) and (8).

$$P_{\text{skin}} = nR_{\text{dc}} F_R(f)\left(\frac{I_L}{n}\right)^2 \tag{7}$$

$$P_{\text{proximity}} = nR_{\text{dc}} G_R(f)(\hat{H}_e^2) \tag{8}$$

where n is the number of strands; R_{dc} is the winding DC resistance; $F_R(f)$ is a factor that describes the increases of DC resistance due to skin effect; $\hat{H}_e$ is the peak of external magnetic field.

2.4. Remaining components models

1. Cooling System: The air-forced cooling system and the single-phase liquid cooling system are both considered in this paper. The defined heatsink geometries for both cooling methods are shown in Fig. 5. The optimizer would sweep through various cooling methods in the optimization process to determine which cooling method has the minimum mass of heatsink while satisfying the temperature constraints. The thermal resistance of the heatsink is calculated using the thermal equivalent circuit method, and the thermal resistance of each semiconductor is extracted from its datasheet. The fluid model in the air-forced cooling system is developed following [21]. The heatsink geometry and fan characteristics are taken into account in the cooling system models. The maximum allowed heatsink thermal resistance is calculated using (9), where the maximum allowed heatsink plate temperature T_{hs} is restricted to 105 ℃ and the maximum ambient temperature T_{amb} is 35 ℃. The mass of the heatsink is calculated based on its geometry.

$$R_{\text{th,hs}} = \frac{T_{\text{hs}} - T_{\text{amb}}}{P_{\text{loss}}} \tag{9}$$

2. Capacitors: Ceramic and film capacitors are considered in this paper due to their high power density and light mass. The method for estimating the mass of capacitors is detailed in (10):

$$m_{\text{cap}} = kV_r^{\alpha} C^{\beta} V_c \tag{10}$$

where k, α, β are parameters related to different types of capacitors and can be found in [22]. The capacitance C, voltage rating V_r, and volume of the capacitor V_c can be extracted from the datasheet.

3. Auxiliary Electronics: Auxiliary electronics include the gate driver, control board, and other auxiliary electronic components in the converter. An auxiliary power of $20W$ [23], denoted as P_{AUX}, and an auxiliary mass of 200g [9], denoted as m_{AUX}, are assumed to be constant in this paper.

3. Single objective optimization

3.1. Optimization routine

The gross mass of the aircraft is set as the objective, considering all relevant degrees of freedom (DOF) in the powertrain system and mission profile. The optimization process employs a hybrid algorithm that integrates the Genetic Algorithm with the Simulated Annealing algorithm (GASA). GASA maintains the rapid global search capability of GA and the local space exploration capability of SA, thereby preventing the algorithm from being trapped in local optima. The lift + cruise aircraft configuration is analyzed in this study, as illustrated in Fig. 6. The total power requirement is evenly distributed across each branch. The objective function can be written as (11):

$$\begin{aligned} &\text{Minimize} && m_{\text{gross}} = f(\mathbf{x}) \\ &\text{Subject to} && p_i(\mathbf{x}) \le 0, i = 1, \ldots, n_p \\ & && m_i(\mathbf{x}) = 0, i = 1, \ldots, n_m \end{aligned} \tag{11}$$

where $f(\mathbf{x})$ is the objective function, subject to n_p inequality constraints $p_i(\mathbf{x})$ and n_m equality constraints $m_i(\mathbf{x})$. The detailed optimization routine is illustrated in Fig. 7.

The design variables, along with other constant inputs, are summarized in Table 3. The lower and upper bounds of the switching frequency are determined by the motor's electrical frequency and the

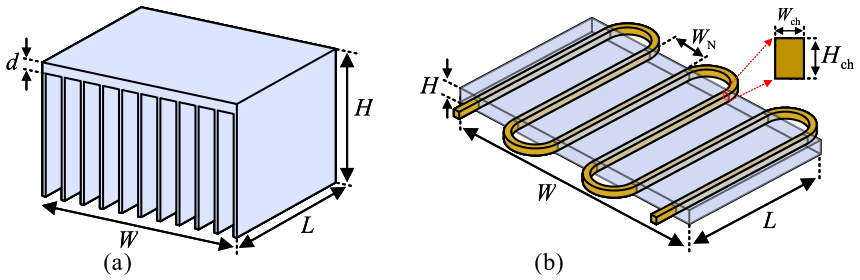

Fig. 5. Defined heatsink geometry. (a) air-forced cooling heatsink. (b) single-phase liquid cold plate.

Table 3
Design variables and constant inputs

Model	Design variable	Variable range	Constant parameters
Powertrain model	Switching frequency, f_{sw}	[10 kHz, 200 kHz]	Motor electric frequency
	DC bus voltage, V_{dc}	[800 V, 1400 V]	Considered semiconductors
	Rated output power, P_o	[40 kW, 1000 kW]	Core material property
	Winding diameter, d_i	[1.4 mm, 4.6 mm]	Capacitor Pk-Pk voltage ripple
	Inductor geometry variables		
	Heatsink geometry variables		
	Ripple attenuation factor, RAF	[0, 1]	
	Inverter Converter topologies, T_i	[1, 3]	
Mass Model	Battery mass, m_{bat}	[400 kg, 800 kg]	Listed in Table 4
Mission model	— —	— —	Listed in Table 4

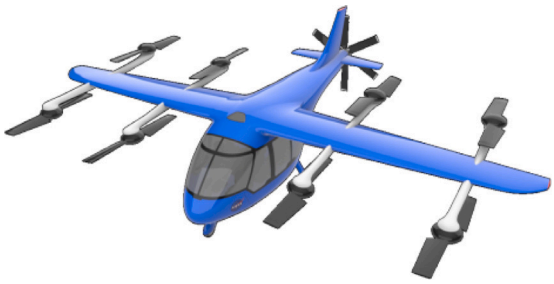

Fig. 6. NASA Lift+Cruise eVTOL aircraft configuration [24].

suitable operating range of WBG devices. In terms of mass minimization, a higher DC bus voltage is preferred [25]. With a constant power requirement, a higher DC bus voltage can reduce cable weight and improve system efficiency. Additionally, the DC bus voltage should vary based on the different sizes and configurations of aircraft. However, the impact of DC bus voltage on the aircraft system has not been systematically studied in the literature. According to a NASA report [26], high-voltage 2 kV+ DC systems enable lightweight, high-efficiency power systems for future electric aircraft. In this paper, considering the state-of-the-art technology, a conservative DC bus voltage of 1400 V is regarded as the upper bound for optimization. During the mission profile, the efficiency of the powertrain can vary with different power demands in each mission segment. Therefore, optimizing the rated output power of the converter is crucial to ensure the highest possible powertrain efficiency throughout the entire mission profile. The range of the rated output power of converter P_o is determined by the aircraft configurations and the potential power range required in the given mission profile. The current density in each conductor is assumed to be between 5 A/mm^2 and 6 A/mm^2 based on empirical data. Given this operating range, the boundary range of winding diameters can be determined. The range of inductor and heatsink geometry variables is based on the dimensions of products currently available on the market. The bound range of converter topologies is defined by the number of converters included in this optimization.

3.2. Mass model

The mass model of the eVTOL aircraft is divided into four components: powertrain mass, battery mass, airframe mass, and motor mass. Motor mass is assumed to be constant in this study. The airframe mass is estimated using a constant airframe mass fraction of the airframe mass to the overall mass of the aircraft. The mass of the powertrain model is the sum of all sub-components mass, as described in Section 2. The battery mass is regarded as a design variable in this optimization. The input parameters of the mass model are shown in Table 4.

3.3. Mission model

The mission model only considers the sizing mission profiles, which mainly emphasize the preliminary design of eVTOL aircraft and the completion of mission tasks, while neglecting the revenues from the mission. A diagram of the mission profile is shown in Fig. 8. Note that only cruise, hover, and reserve mission segments are included in the sizing mission profile. The reserve segment is typically considered to ensure additional battery capacity or flight time for emergency situations. A 20-min reserve time is included in the mission model, following the requirement of visual flight rules (VFR) by the FAA [27]. Moreover, the reserve speed need to be adjusted due to the loiter requirement from FAA. The adjustment method could be found in [4]. The input parameters of the mission model are presented in Table 4.

In order to analyze the performance of powertrain throughout the entire mission profile, the power demand for each mission must be calculated. To maintain the hover state, the rotors have to produce enough thrust equal to aircraft weight during the hover segment, as described in (12). The power of propellers in the hover segment can be calculated using (13) based on momentum theory.

$$NT - W = 0 \tag{12}$$

$$P_h^r = \frac{C_P}{C_T} V_t T \tag{13}$$

where T is the thrust generated by the single rotor, N is the number of rotors, W is the gross weight of aircraft, C_T and C_P are the thrust coefficient and rotor power coefficient, and V_t is the rotor tip speed.

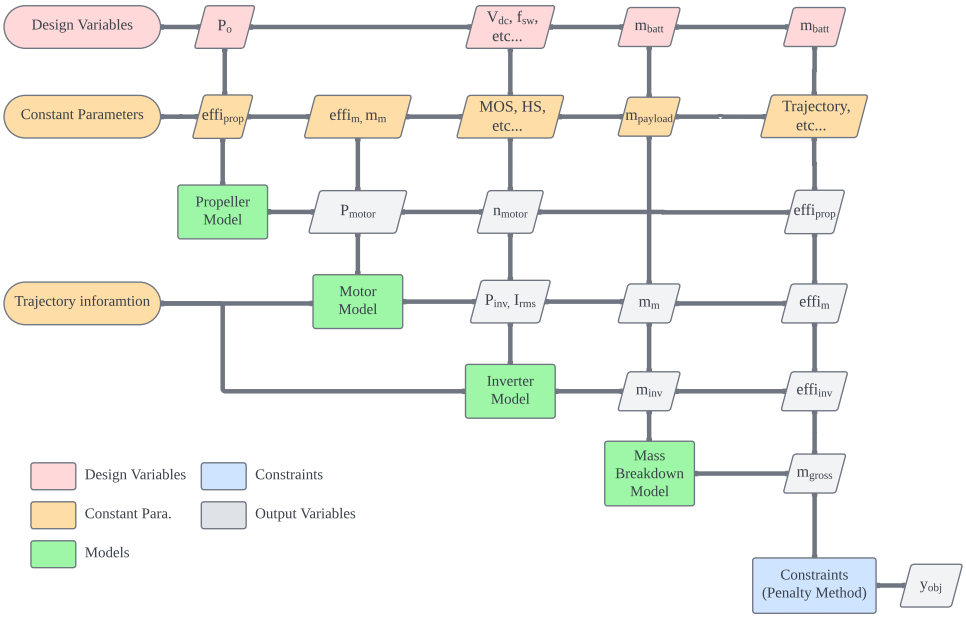

Fig. 7. Optimization flowchart.

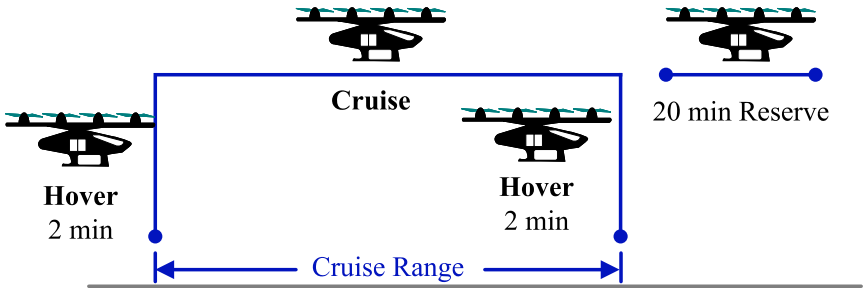

Fig. 8. Sizing mission profile.

Table 4
Input parameters of mission model and mass model

Model	Parameter	Value
Mission model	Cruise mission range	30 km
	Pilot mass	75 kg
	Passengers	3
	Mass per passenger	90 kg
	Reserve time	20 min
	Hover time	2 min
	Cruise speed	124 km/h
	Lift to Drag ratio of cruise	10
	Motor efficiency	95%
	Propeller efficiency	85%
Mass model	Airframe mass fraction	0.53
	Motor mass	25 kg
	Number of motors	8
	Battery energy density	400 Wh/kg

In the cruise and reserve mission segments, the required output power of inverter can be calculated using (14). Due to the loiter adjustment in the reserve segment, the L/D ratio of the reserve needs to be adjusted accordingly [4].

$$P_{\text{inv}}^{i} = \frac{WV_i}{(L/D)_i \eta_{\text{m}} \eta_{\text{p}}}, i = \text{cruise, reserve} \tag{14}$$

where P_{inv}^{i} represents the required output power of the inverter, W is the gross weight of the eVTOL aircraft, L/D is the aircraft's lift-to-drag ratio, η_{m} denotes the motor efficiency, and η_{p} is the propeller efficiency.

Apart from that, the efficiency and power distribution inside the powertrain system can be further calculated using the powertrain model and the given constant motor efficiency in Table 4. Subsequently, the used battery energy in each mission segment can be calculated using (15).

$$E_{\text{i}} = \frac{P_i t_i}{\eta_i} \tag{15}$$

where i represents the different mission segments, P_i and η_i represent the output power and efficiency of the powertrain, respectively, while t_i is the flight time of each mission segment.

An equality constraint is used in the mission model, as shown in (16), to ensure appropriate energy distribution throughout the mission task.

$$E_{\text{b}} - (E_{\text{h}} + E_{\text{c}} + E_{\text{r}}) = 0 \tag{16}$$

where E_{b} represents the total battery energy, E_{h} is the energy used in the hover segment, E_{c} is the energy used in the cruise segment, and E_{r} is the energy used in the reserve segment.

Since the battery mass is considered as a design variable, the total battery energy, E_b, can be calculated by multiplying the battery mass by the constant battery energy density provided in Table 4.

4. Results and discussion

4.1. Powertrain model validation

The powertrain model has been validated through a comparison with simulation results obtained from the PSIM software. A 60 kW

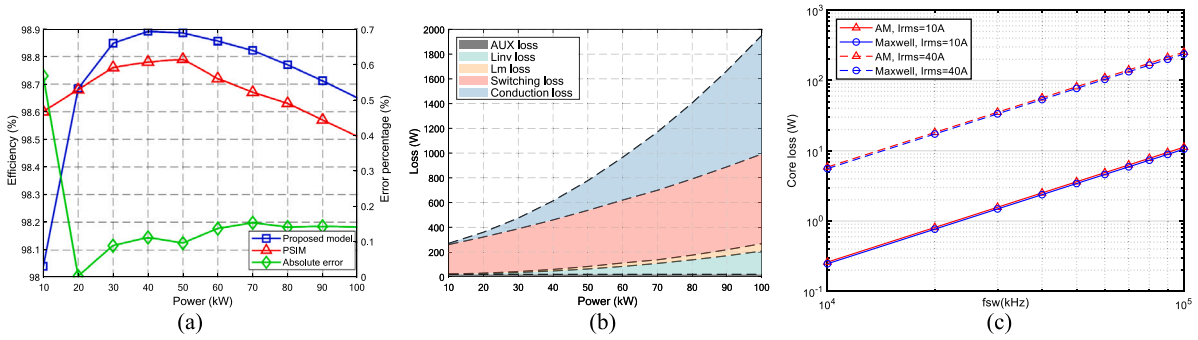

Fig. 9. Validation results for the powertrain model. (a) the comparison of efficiency. (b) loss breakdown with the increasing power demand. (c) the comparison of core losses between AM and Maxwell under various load conditions.

3L-ANPC inverter was used to validate the powertrain model. The non-ideal thermal switch model was utilized in this simulation. Fig. 9(a) shows the efficiency comparison between the proposed powertrain model and the PSIM simulation, and the absolute error is also presented in this figure. In the 10 kW case, due to the non-linear effect on the switching losses, the powertrain model cannot estimate efficiency accurately. The absolute errors at higher power levels are similar. This is because the core losses of each inductor are only considered in the proposed powertrain model. The errors in switching losses and conduction losses gradually increase with higher power demand. Fig. 9(b) illustrates the loss breakdown in the powertrain model, where the switching and conduction losses constitute the majority of the power losses. The inductor core loss is validated by Ansys Maxwell software. Fig. 9(c) shows the comparison of core losses under different load between the analytical model (AM) and Ansys Maxwell's simulation. MnZn ferrite N87 material was used. Its datasheet and parameters are detailed in [18].

4.2. Optimization results

The input data for this optimization study is given by Tables 3 and 4. The key results of this optimization study are shown in Fig. 10, where the mass of powertrain, battery, motor, airframe, and crews and passengers are considered in this optimization problem. Fig. 10(a) shows the optimization results for the gross mass minimization. As discussed in the previous section, the GA algorithm is primarily used for rapidly searching for potential optimal solutions in the first 400 generations. After that, due to the existence of multiple local optimum solutions, the SA algorithm, combined with the GA, is used to find potential optimal solutions efficiently. The gross mass is gradually reduced and converged in the last few generations. Fig. 10(b) shows the optimization results of total powertrain mass.

Figs. 10(c), 10(d), and 10(e) show the variation of design variables during the optimization process. The 3L-ANPC inverter is selected since it theoretically has the highest efficiency among all inverter topologies in high power and high voltage applications. The switching frequency and DC bus voltage are converged at 116 kHz and 1400 V, respectively. This would be the optimal selection by the optimizer, considering the trade-off between powertrain efficiency and the total system mass. A higher switching frequency would reduce the mass of passive components but also increase losses. The DC bus voltage approaches the upper bound mainly because conduction losses can be reduced at the same power level of the powertrain system. The other design variables have converged at a certain level, and none of the constraints are violated in the final optimization results. The battery mass is converged at 589 kg, and the efficiency of powertrain and output power of propeller in each mission segment are shown in Fig. 10(f). The reserve segment has the lowest required power due to the loiter adjustments discussed in Section 3.2. The hover segment has the highest power and lowest efficiency.

4.3. Comparison study

The comparison in this section is based on the optimized results and data shown in [4]. The author in [4] implemented the optimization of eVTOL aircraft, without powertrain modeling. The author also presented data on the mass of the aircraft, mass of the battery, and the distribution of output power in each mission segment. This study utilizes the identical input data as the lift+cruise eVTOL aircraft in [4], and focuses on optimizing the gross mass of the eVTOL aircraft. Finally, a comparison is made between the mass of the eVTOL aircraft, the amount of required battery energy, and the distribution of output power in each mission segment. Since the motor mass and powertrain mass are neglected in [4], these mass are also ignoring in this comparison study.

In this comparison, a 56 km mission range, including the cruise and reserve mission range, is assumed for this mission profile. The vehicle cruise speed and time distribution of each segment are fixed. Fig. 11(a) illustrates that the battery mass is 8.76% lighter than the reference battery mass. A 4.3% reduction in overall mass is accomplished through powertrain optimization. Fig. 11(b) shows that almost 8.76% decrease in battery energy consumption during the whole mission profiles, in comparison to the reference data. Fig. 11(c) shows the comparison of battery power distribution among the three categories of mission section. The required power in each segment is less than the reference value. These improvements are contributed by the improved powertrain efficiency and optimized energy distribution for each segment. It is theoretically true because the overall efficiency in the electric system is improved by the powertrain optimization, the total required battery energy could be reduced. In our proposed model, the overall efficiency of the powertrain and motor increased from 90% to 93.4%. Theoretically, the battery mass should be reduced by 3.6%. However, there was a up to 8.76% reduction in the mass of the battery. This is because the trajectory optimization also contributes to the reduction of battery mass in this case. Once the battery mass is reduced, the gross weight of the aircraft correspondingly decreases. As a result, the range constraints in (14) are not satisfied with the reduced gross weight. Eq. (14) can also be formed as (17).

$$\text{Range}_i = \eta_{\text{sys,i}} \frac{L}{D} \frac{\frac{P_i t_i}{\eta_{\text{sys,i}}}}{W} = \frac{L}{D} \frac{P_i t_i}{W} \tag{17}$$

The range constraints are directly related to the output power in each segment and the gross weight of the aircraft. When the gross weight is reduced, the optimizer must decrease the output power of each segment to maintain a constant range. Consequently, the battery mass is further reduced. It should be noted that the reduction in airframe mass also contributes to the total mass reduction in the final optimization results, owing to the fixed airframe mass ratio.

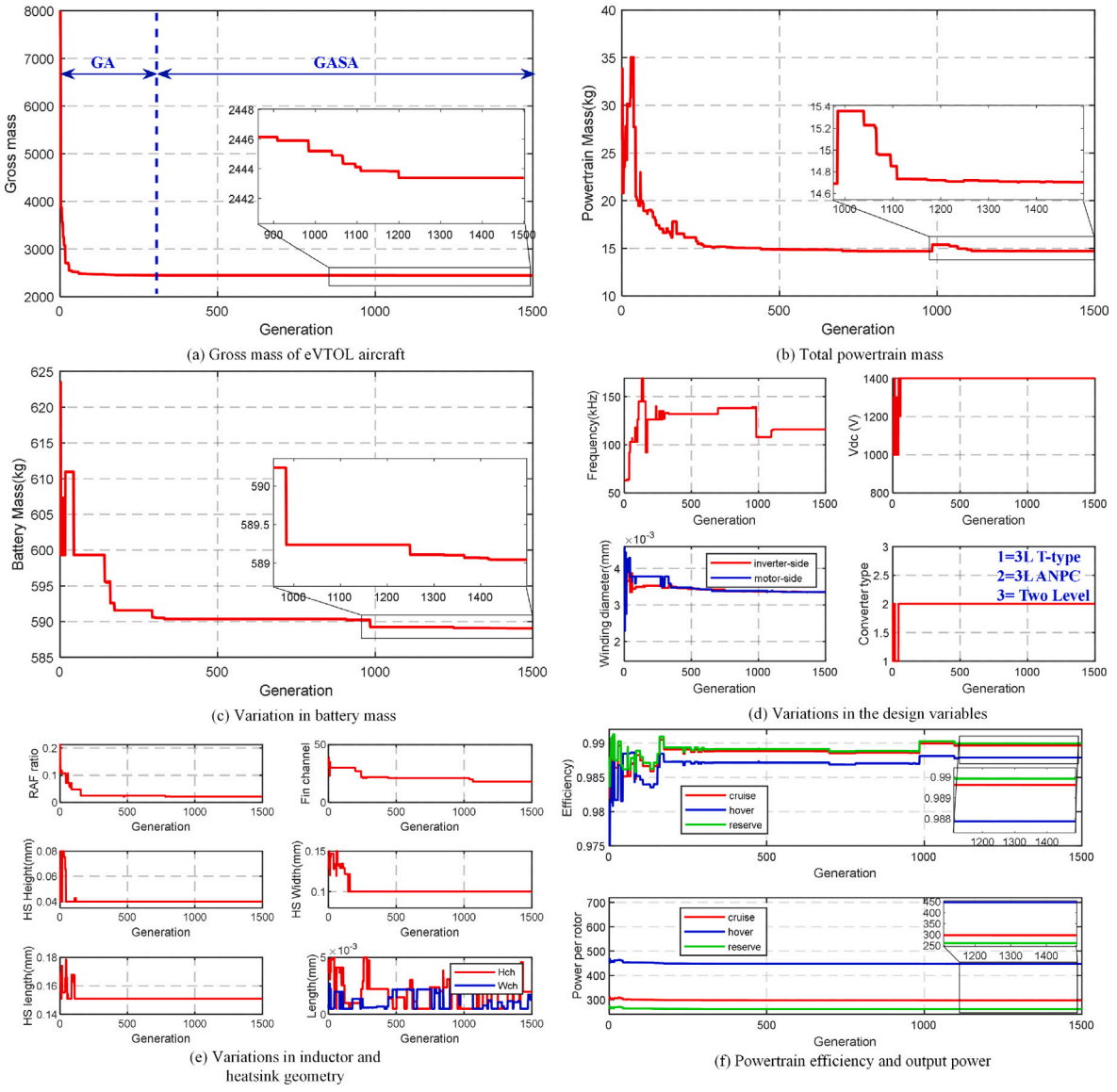

Fig. 10. Results from the configuration study. (a) gross mass of eVTOL aircraft. (b) total powertrain mass. (c) variation in the design variables of battery mass. (d) variations in the design variables of switching frequency, DC bus voltage, winding diameters on the inductor, and discrete converter type. (e) variations in the design variables of inductor and heatsink geometry. (f) powertrain efficiency and output power of the propeller in each mission segment.

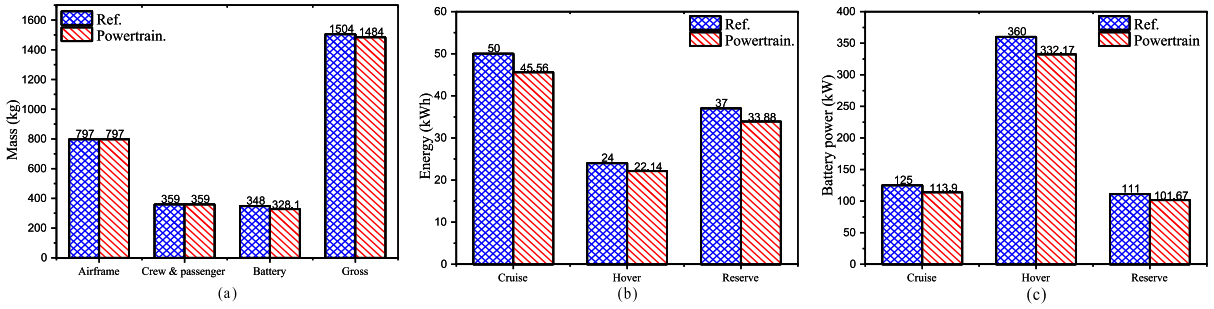

Fig. 11. Results of the comparison between optimization without powertrain model and with powertrain model. (a) Mass breakdown. (b) Energy consumption. (c) Battery power draw.

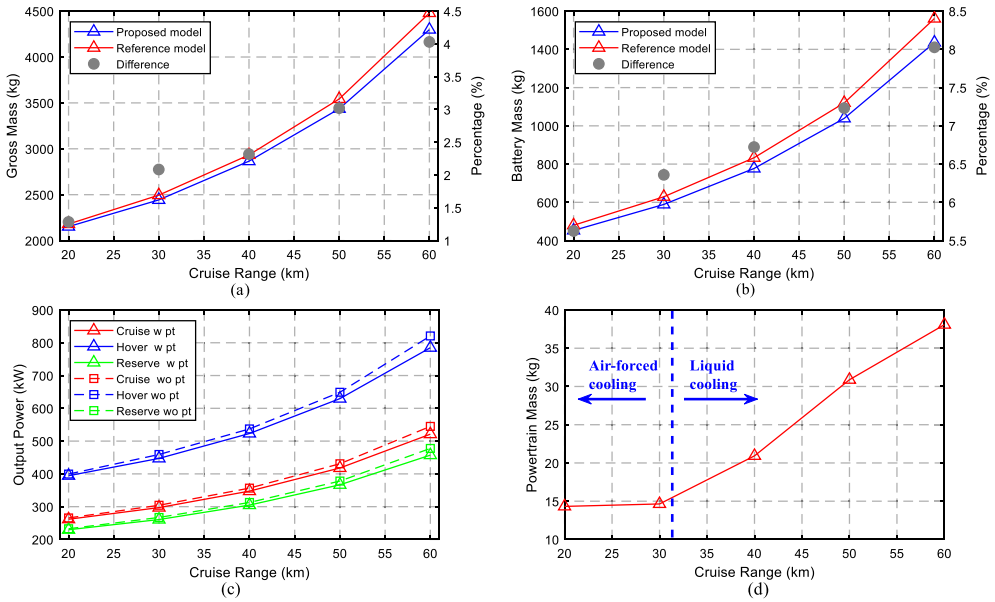

Fig. 12. Sensitivity to cruise mission range. (a) gross mass of eVTOL aircraft. (b) battery mass. (c) output power of each segment. (d) powertrain mass.

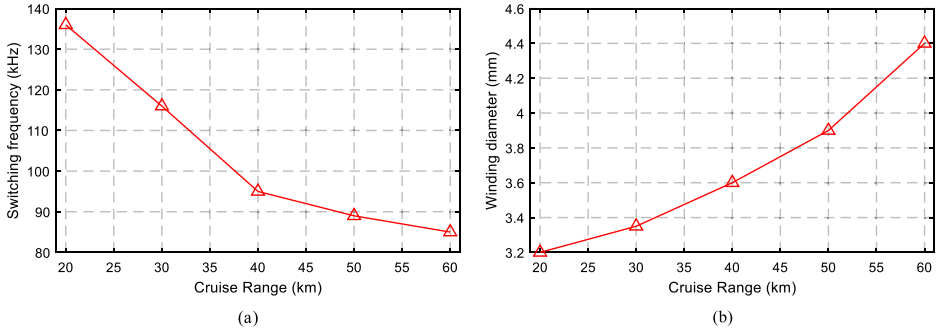

Fig. 13. Sensitivity to mission range. (a) switching frequency. (b) winding diameter.

4.4. Sensitivity analysis

The sensitivity of the mission range is analyzed by varying the cruise mission range and optimizing the gross mass of the eVTOL aircraft accordingly. The same input parameters and mass model from the optimization study are used in this analysis. Key results are illustrated in Figs. 12 and 13.

Figs. 12(a) and 12(b) illustrate the variations in gross mass and battery mass with respect to the mission range, including a comparison between models with and without a powertrain. As the mission range increases, the impact of the powertrain on both the gross mass and the battery mass of the eVTOL becomes increasingly profound. Fig. 12(c) presents the variation of output power across different mission segments, with a comparison between models with and without a powertrain. The optimization of output power of the powertrain in each segment is achieved through the powertrain model. Furthermore, Fig. 12(d) highlights a notable increase in the mass of the powertrain after 30 km cruise range. This increase is attributed to the inadequacy of air-forced cooling to meet the thermal constraints after 30 km, necessitating the use of the liquid cooling method.

Fig. 13(a) illustrates the trend in switching frequency as the mission range increases. This is because the power demand of each segment gradually increases with the longer mission range, while the DC bus voltage remains constant, leading to an increased current in the converter. Consequently, the conduction losses are further increased. To maintain high efficiency of the powertrain, the optimizer captures this characteristic and gradually decreases the switching frequency to compensate for the increase in conduction losses. Fig. 13(b) demonstrates the variation in winding diameter. Due to the gradual increase in power demand, the current also increases. Therefore, a larger winding diameter is required to maintain the appropriate current density throughout the mission profile.

5. Conclusion

This work proposes a conceptual design and optimization methodology for eVTOL aircraft, focusing on the powertrain aspect. While most eVTOL aircraft optimizations either neglect the powertrain model or rely on basic equation-based models, this study breaks new ground by offering a comprehensive powertrain modeling methodology. It also performs a comparative study of models with and without a powertrain. This method is designed to underscore the critical role of powertrain considerations in the optimization process for eVTOL aircraft design.

This proposed comprehensive powertrain modeling methodology includes the following aspects: (1) Different converter topologies are discussed and analyzed. (2) A mathematical model for calculating losses is introduced. (3) The detailed selection of semiconductor devices is discussed. (4) A comprehensive analysis of magnetic components is provided, which includes an in-depth analysis of various magnetic materials and their suitability for specific applications. (5) Methods for air-forced cooling and single-phase liquid cooling are presented. (6) The selection of capacitors is also explored, highlighting their significance and applications within the powertrain system.

A combined GASA optimization algorithm is utilized in this optimization problem. A configuration study of a 30 km cruise range case and a comparison study are conducted in this work. The comparative analysis reveals that the proposed model is capable of achieving up to a 4.3% reduction in gross mass through powertrain and trajectory optimization. Sensitivity to mission range is analyzed. It is observed that the impact of the powertrain on the eVTOL aircraft becomes more profound with an increase in range.

This paper quantitatively evaluates the influence of the powertrain system on eVTOL aircraft across various applications. Additionally, a detailed powertrain modeling methodology is introduced, aiming to provide guidance for individuals without a background in power electronics on constructing powertrain models for interdisciplinary applications. The system-level powertrain modeling framework could be further expanded by incorporating detailed battery models and capturing transient behaviors of both motors and converters. Such enhancements would provide a more comprehensive understanding of dynamic performance and interactions within the complete powertrain system and have an insight of powertrain performance through the entire mission profile.

CRediT authorship contribution statement

Zeyu Cheng: Writing – original draft, Visualization, Validation, Software, Methodology, Formal analysis, Conceptualization. **Zhi Cao:** Writing – review & editing. **John T. Hwang:** Writing – review & editing, Supervision, Project administration, Funding acquisition. **Chris Mi:** Writing – review & editing, Supervision, Funding acquisition.

Declaration of competing interest

The authors declare the following financial interests/personal relationships which may be considered as potential competing interests: Zeyu Cheng reports financial support was provided by NASA under award No. 80NSSC21M0070 If there are other authors, they declare that they have no known competing financial interests or personal relationships that could have appeared to influence the work reported in this paper.

Data availability

No data was used for the research described in the article.

References

[1] Moore Mark D. Concept of operations for highly autonomous electric zip aviation. In: 12th AIAA aviation technology, integration, and operations (ATIO) conference. 2012, p. 1–15.

[2] Asmer Lukas, Pak Henry, Prakasha Prajwal S, Schuchardt Bianca I, Weiand Peter, Meller Frank, et al. Urban air mobility use cases, missions and technology scenarios for the horizonuam project. In: AIAA aviation 2021 forum. 2021, p. 3198.

[3] Boretti Alberto. Advantages of plug-in hybrid electric vertical take-off and landing aircraft with hydrogen energy storage. Int J Hydrog Energy 2024;55:339–46.

[4] Brown Arthur, Harris Wesley L. Vehicle design and optimization model for urban air mobility. J Aircr 2020;57(6):1003–13.

[5] Scholz Anna Elena, Trifonov Dimitar, Hornung Mirko. Environmental life cycle assessment and operating cost analysis of a conceptual battery hybrid-electric transport aircraft. CEAS Aeronaut J 2022;13(1):215–35.

[6] Critchfield Tyler, Ning Andrew. Low-fidelity design optimization and parameter sensitivity analysis of tilt-rotor eVTOL electric propulsion systems. In: AIAA SCITECH 2023 forum. 2023, p. 0325.

[7] Orndorff Nicholas C, Sarojini Darshan, Scotzniovsky Luca, Gill Hyunjune, Lee Seongkyu, Cheng Zeyu, Zhao Shuofeng, Mi Chris, Hwang John T. Air-taxi transition trajectory optimization with physics-based models. In: AIAA SCITECH 2023 forum. 2023, p. 0324.

[8] Ruh Marius L, Fletcher Andrew, Sarojini Darshan, Sperry Mark, Yan Jiayao, Scotzniovsky Luca, et al. Large-scale multidisciplinary design optimization of a NASA air taxi concept using a comprehensive physics-based system model. In: AIAA SCITECH 2024 forum. 2024, p. 0771.

[9] Menzi David, Imperiali Luc, Bürgisser Elias, Ulmer Martin, Huber Jonas, Kolar Johann W. Ultra-lightweight high-efficiency buck-boost DC-DC converters for future eVTOL aircraft with hybrid power supply. IEEE Trans Transp Electrification 2024.

[10] Nawawi Arie, Tong Chin Foong, Yin Shan, Sakanova Assel, Liu Yitao, Liu Yong, et al. Design and demonstration of high power density inverter for aircraft applications. IEEE Trans Ind Appl 2016;53(2):1168–76.

[11] Lee Donguk, Lim Daejin, Yee Kwanjung. Generic design methodology for vertical takeoff and landing aircraft with hybrid-electric propulsion. J Aircr 2022;59(2):278–92.

[12] Kim Hojin, Lee Jinwhuy, Lee Donguk, Yee Kwanjung. Improved conceptual design of eVTOL aircraft: Considering rotor–rotor interactional effects. Int J Aeronaut Space Sci 2025;1–20.

[13] Clarke Sean, Redifer Matthew, Papathakis Kurt, Samuel Aamod, Foster Trevor. X-57 power and command system design. In: 2017 IEEE transportation electrification conference and expo. IEEE; 2017, p. 393–400.

[14] Liu Yong, See Kye-Yak, Yin Shan, Simanjorang Rejeki, Tong Chin Foong, Nawawi Arie, et al. LCL filter design of a 50-kW 60-kHz SiC inverter with size and thermal considerations for aerospace applications. IEEE Trans Ind Electron 2017;64(10):8321–33.

[15] Sarojini Darshan, Ruh Marius, Yan Jiayao, Scotzniovsky Luca, Orndorff Nicholas C, Xiang Ru, et al. Review of computational models for large-scale MDAO of urban air mobility concepts. In: AIAA sciTech 2024 forum. 2024, p. 0377.

[16] Ouyang Ziwei, Andersen Michael AE. Overview of planar magnetic technology—Fundamental properties. IEEE Trans Power Electron 2013;29(9):4888–900.

[17] Li Jieli, Abdallah Tarek, Sullivan Charles R. Improved calculation of core loss with nonsinusoidal waveforms. In: Conference record of the 2001 IEEE industry applications conference. 36th IAS annual meeting (cat. no. 01CH37248), vol. 4, IEEE; 2001, p. 2203–10.

[18] National Energy Technology Laboratory. Core-loss datasheet MnZn Ferrite N87. Technical report, DOE; 2018, DOE.

[19] National Energy Technology Laboratory. METGLAS-2605-SA1 core-loss datasheet. Technical report, DOE; 2018.

[20] Mühlethaler Jonas. Modeling and multi-objective optimization of inductive power components [Ph.D. thesis], ETH Zurich; 2012.

[21] Gammeter Christoph, Krismer Florian, Kolar Johann W. Weight optimization of a cooling system composed of fan and extruded-fin heat sink. IEEE Trans Ind Appl 2014;51(1):509–20.

[22] Zou Jiarui, Brooks Nathan C, Coday Samantha, Ellis Nathan M, Pilawa-Podgurski Robert CN. On the size and weight of passive components: Scaling trends for high-density power converter designs. In: 2022 IEEE 23rd workshop on control and modeling for power electronics. IEEE; 2022, p. 1–7.

[23] Burkart Ralph M, Kolar Johann W. Comparative $\eta-\rho-\sigma$ Pareto optimization of Si and SiC multilevel dual-active-bridge topologies with wide input voltage range. IEEE Trans Power Electron 2016;32(7):5258–70.

[24] Silva Christopher, Johnson Wayne. Practical conceptual design of quieter urban VTOL aircraft. In: Vertical flight society's 77th annual forum & technology display. 2021.

[25] Dorn-Gomba Lea, Ramoul John, Reimers John, Emadi Ali. Power electronic converters in electric aircraft: Current status, challenges, and emerging technologies. IEEE Trans Transp Electrification 2020;6(4):1648–64.

[26] Dyson Rodger. Current status and future plans for electric motors and drives at NASA. In: 2021 IEEE international electric motors and drives conference. 2021.

[27] Deptof Transportation, Federal Aviation Administration. 14 CFR 91.151—Fuel requirements for flight in VFR conditions. Washington, D.C.; 2017, https://www.law.cornell.edu/cfr/text/14/91.151. [Retrieved 14 August 2019].